Supporting Information for

Ultrascalable Three-Tier Hierarchical Nanoengineered Surfaces for Optimized Boiling

Jiaqi Li,[†] Wuchen Fu,[†] Bohan Zhang,[†] Gaohua Zhu,[‡] Nenad Miljkovic[,†,§,∥,#]*

[†]*Department of Mechanical Science and Engineering, University of Illinois, Urbana, Illinois 61801, United States*

[‡]*Materials Research Department, Toyota Research Institute of North America, Ann Arbor, Michigan 48105, United States*

[§]*Department of Electrical and Computer Engineering, University of Illinois, Urbana, Illinois 61801, United States*

[∥]*Materials Research Laboratory, University of Illinois, Urbana, Illinois 61801, United States*

[#]*International Institute for Carbon Neutral Energy Research (WPI-I2CNER), Kyushu University, 744 Moto-oka Nishi-ku, Fukuoka 819-0395, Japan*

*Corresponding author. E-mail: nmiljkov@illinois.edu

S1. Supplementary Videos

Video S1: Water vapor bubble behavior on the unmodified surface near the onset of nucleate boiling (ONB), where the surface heat flux q'' ≈ 4.7 W/cm^2. The sample size is 15 mm x 15 mm. The video was captured with a high-speed camera (Photron Mini AX 200) and a high magnification zoom lens (InfiniProbe TS-160) with a downward angle of ≈5º. The video was captured at 2000 fps and is played back at 30 fps.

Video S2: Water vapor bubble behavior on the modified structured hierarchical surface having deposition time t_d = 5 s near the onset of nucleate boiling (ONB), where the surface heat flux q'' ≈ 3.7 W/cm^2. The sample size is 15 mm x 15 mm. The video was captured with a high-speed camera (Photron Mini AX 200) and a high magnification zoom lens (InfiniProbe TS-160) with a downward angle of ≈5º. The video was captured at 2000 fps and is played back at 30 fps.

Video S3: Water vapor bubble behavior on modified structured hierarchical surface having deposition time t_d = 10 s near the onset of nucleate boiling (ONB), where the surface heat flux q'' ≈3.3 W/cm^2. The sample size is 15 mm x 15 mm. The video was captured by a high-speed camera (Photron Mini AX 200) and a high magnification zoom lens (InfiniProbe TS-160) with a downward angle of ≈5º. The video was captured at 2000 fps and is played back at 30 fps.

Video S4: Water vapor bubble behavior on modified structured hierarchical surface having deposition time t_d = 20 s near the onset of nucleate boiling (ONB), where the surface heat flux q'' ≈2.9 W/cm^2. The sample size is 15 mm x 15 mm. The video was captured by a high-speed

camera (Photron Mini AX 200) and a high magnification zoom lens (InfiniProbe TS-160) with a downward angle of ≈5º. The video was captured at 2000 fps and is played back at 30 fps.

Video S5: Water vapor bubble behavior on modified structured hierarchical surface having deposition time t_d = 30 s near the onset of nucleate boiling (ONB), where the surface heat flux q'' ≈1.2 W/cm^2. The sample size is 15 mm x 15 mm. The video was captured by a high-speed camera (Photron Mini AX 200) and a high magnification zoom lens (InfiniProbe TS-160) with a downward angle of ≈5º. The video was captured at 2000 fps and is played back at 30 fps.

Video S6: Water vapor bubble behavior on modified structured hierarchical surface having deposition time t_d = 40 s near the onset of nucleate boiling (ONB), where the surface heat flux (q'') are ≈3.2 W/cm^2. The sample size is 15 mm x 15 mm. The video was captured by a high-speed camera (Photron Mini AX 200) and a high magnification zoom lens (InfiniProbe TS-160) with a downward angle of ≈5º. The video was captured at 2000 fps and is played back at 30 fps.

Video S7: Top-view endoscopic video of the water vapor bubble growth process on modified structured hierarchical surface having deposition time t_d = 20 s near the onset of nucleate boiling (ONB), where the surface heat flux q'' ≈2.21 W/cm^2. The average diameter of the pore is ≈44 μm. The video was captured vertically by a high-speed camera (Photron Mini AX 200) and a high magnification zoom endoscope (HawKeye Pro Hardy 17″). The video was captured at 4000 fps and is played back at 15 fps.

Video S8: H_2 bubble growth behavior on vertically oriented copper cathode during the cathodic deposition process. The current density is 3A/cm^2. The sample size is 10 mm x 10 mm. The video was captured with a high-speed camera (Photron Mini AX 200) and a high magnification zoom lens (InfiniProbe TS-160) horizontally. The video was captured at 2000 fps and is played back at 30 fps.

S2. Surface Preparation

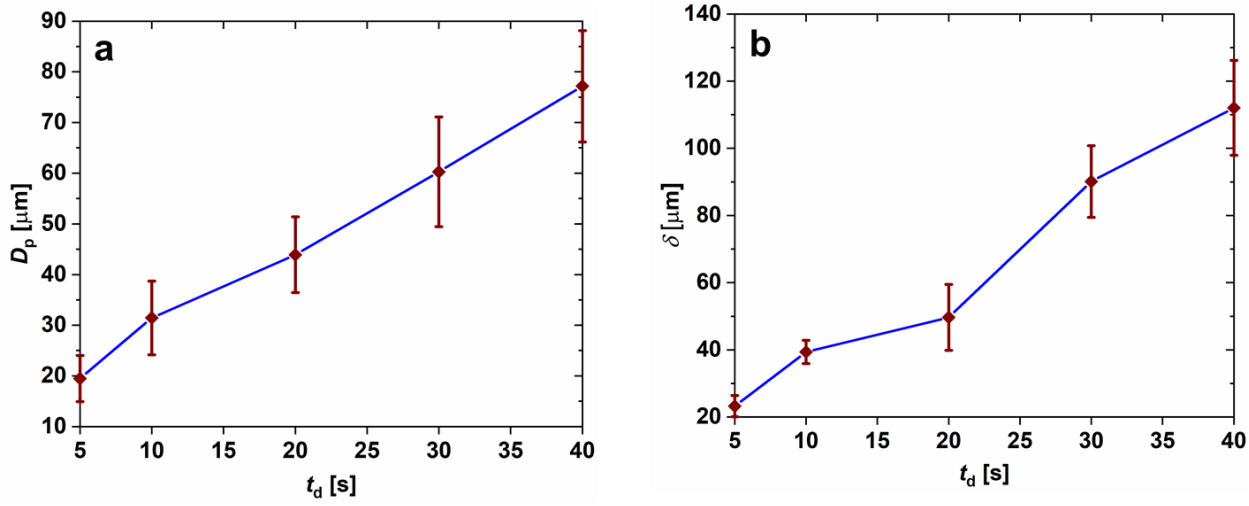

Figure S1. Variation of (a) pore size (D_p) and (b) layer thickness (δ) of the cathodic deposition structures as a function of deposition time, t_d. Error bars represent one standard deviation between 10 measurements conducted at different spatial locations on each sample.

S3. Surface Porosity Estimation

The porosity of the fabricated hierarchical structured surfaces was determined using area estimation after binarization of top-view SEM images using ImageJ software. Threshold of the binarization was carried out visually using the default setting and manually adjusting to incorporate the maximum degree of observed porosity. An exemplary result of binarization is shown in Fig. S2, with summarized results for all surfaces in Table S1. Considering the uncertainty associated with standard deviation between different spatial regions, the porosity of samples having different deposition times was remarkably similar.

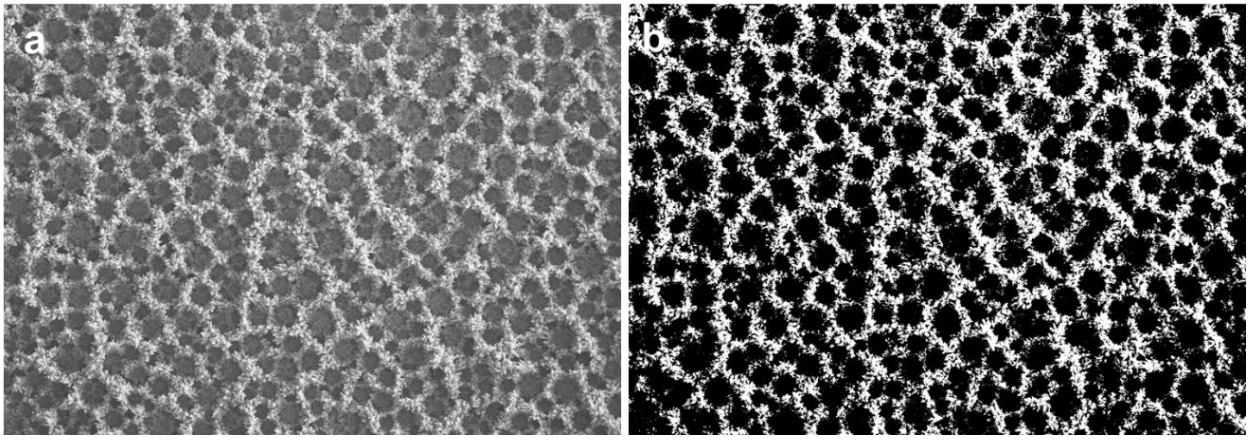

Figure S2. Comparison of top-view scanning electron microscopy images (a) before and (b) after binarization using ImageJ software.

Table S1. Porosity values of samples as a function of deposition time.

Deposition time (s)	**5**	**10**	**20**	**30**	**40**
Porosity (%)	70.6 ± 2.4	70.5 ± 3.1	71.4 ± 2.7	71.5 ± 1.8	71.4 ± 1.6

S4. Droplet Spreading Phenomena on Superhydrophilic Surfaces

All the fabricated hierarchical structured surfaces are superhydrophilic. As shown in Fig. S3, when the droplet contacts the surfaces, it spreads into a liquid film within 0.3 s, and the static contact angle is nearly zero.

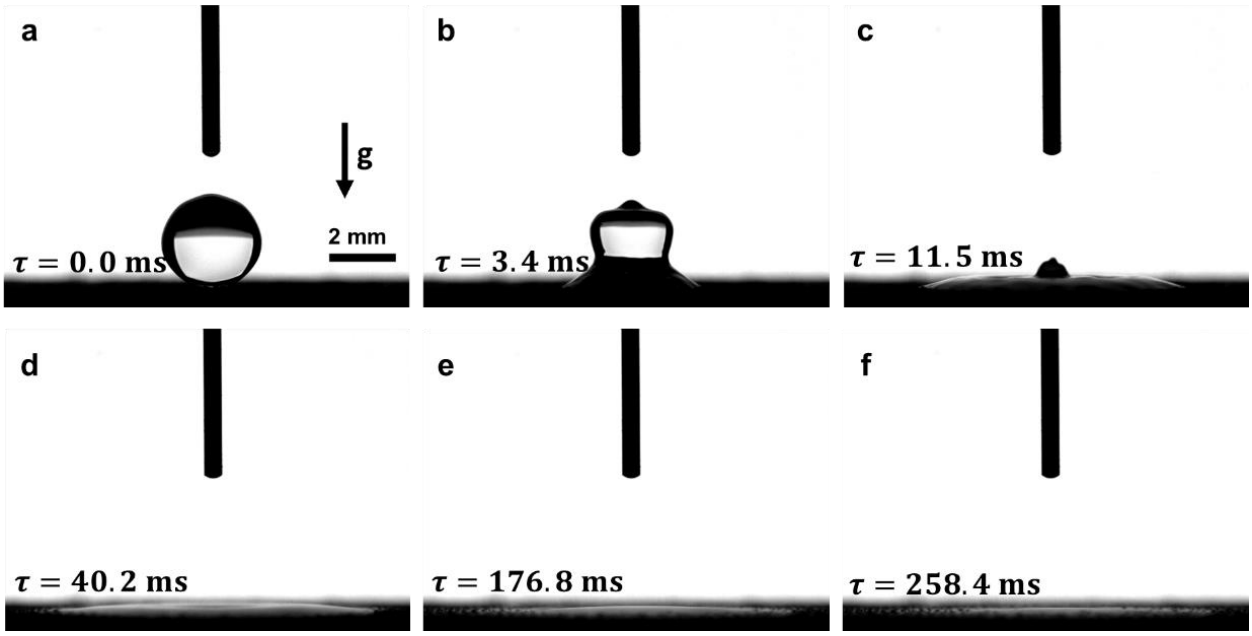

Figure S3. Water droplet spreading phenomena on our structured superhydrophilic surfaces. The structured surface was obtained using a deposition time of 5 s.

S5. Surface Wickability Measurement

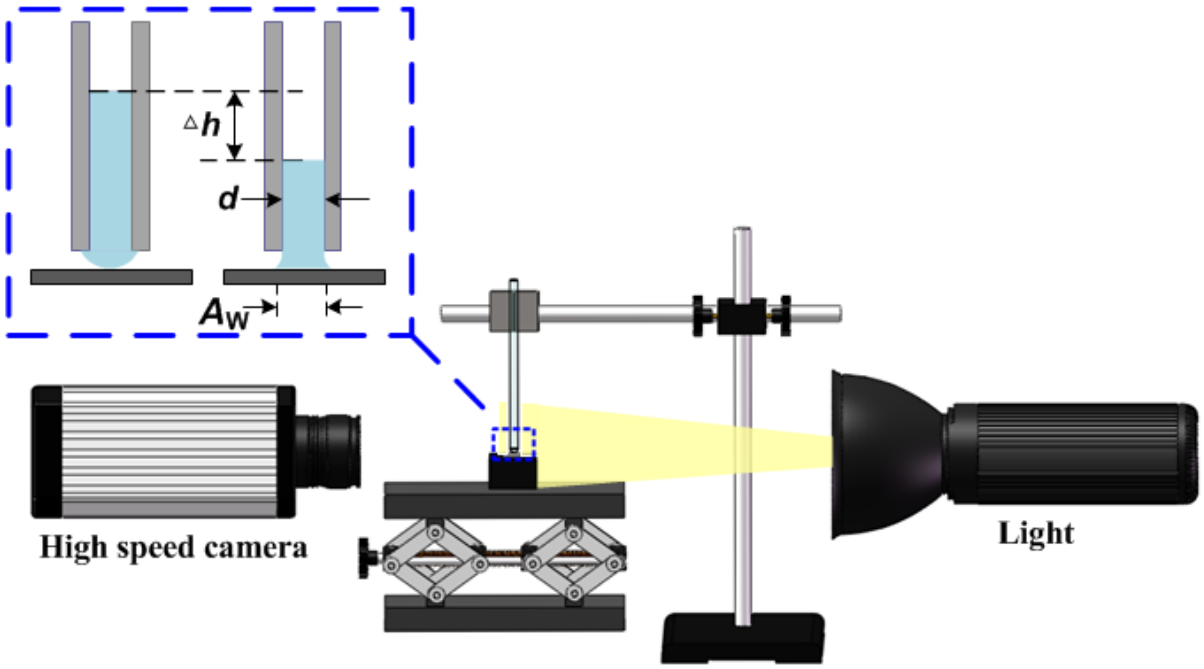

Figure S4. Schematic of the surface wickability measurement setup.

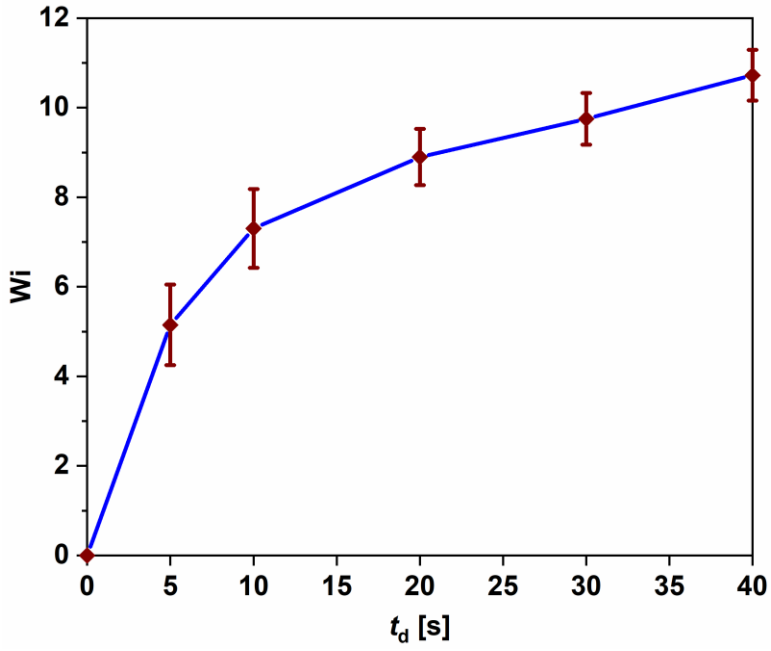

Figure S5. Surface dimensionless wickability Wi as a function of deposition time t_d. Error bars were computed using propagation of error on the measured quantities.

S6. Repeatability and Error Analysis during Pool Boiling Tests

The test the repeatability of the pool boiling behavior as well as the soldering procedure, three separate tests were done on three unmodified surfaces. The acquired pool boiling and HTC curves for the three tests are shown in Figure S6, showing good repeatability.

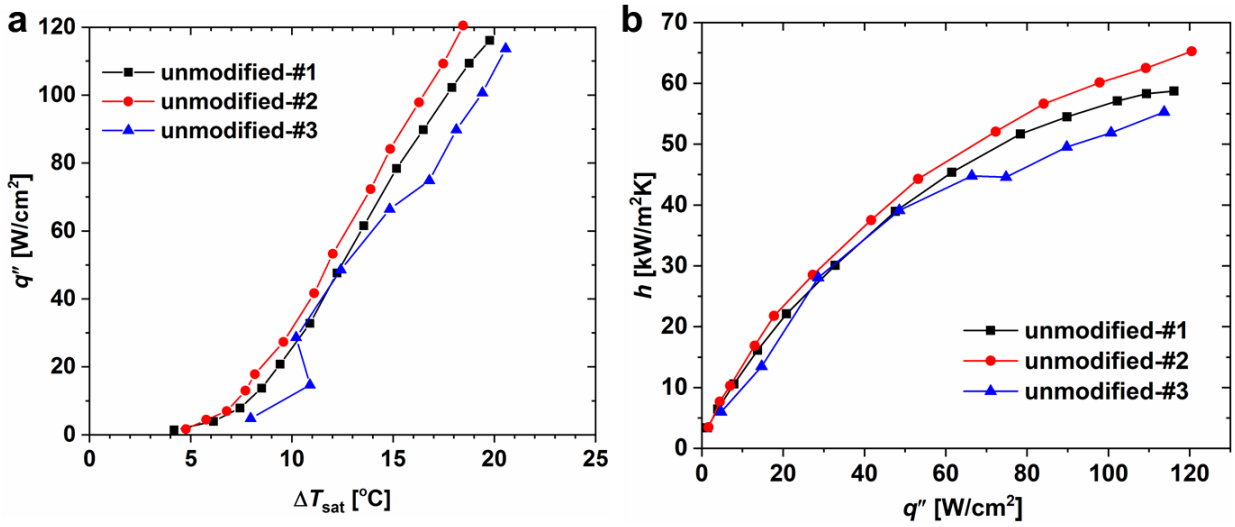

Figure S6. (a) Surface pool boiling heat flux (q") as a function of wall superheat ($T_{\text{surface}} - T_{\text{sat}}$), and (b) HTC as a function of (q") during the repeatability tests on 3 separate unmodified samples. Error bars not shown for clarity.

All temperatures were measured using K-type thermocouples (TJC36-CAIN-020(G)-6, OMEGA) which were calibrated using a high-accuracy Class AA reference resistance temperature detector (RTD, B-PX1126Y-LR4P39T2S, Reotemp Instruments) sensor with a maximum measurement error of ± 0.1°C. The surface heat flux and temperature were calculated using Eqs. (4) and (5) of manuscript, respectively. The errors stem from the measurement error of temperature and distance between two adjacent thermocouples. The uncertainty of q" and T_{surface} can be estimated through error propagation:[1]

$$\frac{U_{q"}}{q"} = \sqrt{\left(\frac{U_{(3T_1-4T_2+T_3)}}{3T_1-4T_2+T_3}\right)^2 + \left(\frac{U_{\Delta x}}{\Delta x}\right)^2}, \quad \text{(S1)}$$

$$\frac{U_{T_{\text{surface}}}}{T_{\text{surface}}} = \sqrt{\left(\frac{U_{T_1}}{T_{\text{surface}}}\right)^2 + \left(\frac{\Delta x\, U_{q"}}{k\, T_{\text{surface}}}\right)^2 + \left(\frac{q"U_{\Delta x}}{k\, T_{\text{surface}}}\right)^2}, \quad \text{(S2)}$$

where $U_{q"}$, $U_{(3T_1-4T_2+T_3)}$, $U_{\Delta x}$ and $U_{T_{\text{surface}}}$ are the uncertainties of heat flux ($q"$), temperature difference ($3T_1-4T_2+T_3$), distance between the thermocouples (Δx), and surface temperature T_{surface}, respectively. The maximum uncertainties of surface heat flux and surface temperature occurred near CHF, which were ± 11.3 W/cm^2 and ± 4.7°C, respectively.

S7. Scaling of the CHF and Bubble Behavior

The bubble departure diameter (D_d) and departure frequency (f) are two key parameters that govern pool boiling performance and determine CHF. The bubble departure diameter is mainly controlled by the balance between the buoyant and surface tension forces acting on the bubble during growth. The buoyant force acts to drive the bubble away from the surface, while the surface tension force acts to keep the bubble attached on the surface. The bubble departure diameter has been shown to scale with the surface wettability and fluid properties as[2]:

$$D_\mathrm{d} \sim \theta \sqrt{\frac{\sigma}{g(\rho_\mathrm{l} - \rho_\mathrm{v})}}\ , \tag{S3}$$

where θ is the apparent receding contact angle on the boiling surface. Intuitively, D_d decreases with lower θ. The hierarchical surfaces developed here are superhydrophilic, exhibiting contact angles approaching zero, reducing the departure diameter significantly. In order to balance the heat removal, a surface with smaller D_d generates more bubbles, that is, f increases. The bubble departure frequency during nucleate pool boiling has been shown to scale as the inverse of the departure diameter:[3]

$$D_\mathrm{d} f \sim \left[\frac{g\sigma(\rho_\mathrm{l} - \rho_\mathrm{v})}{\rho_\mathrm{l}^2}\right]^{\frac{1}{4}}, \tag{S4}$$

It is well known that the ONB, identified by the observation of first bubbles on the heated surface, is the point where the heat transfer mode changes from single-phase natural convection to nucleate pool boiling[3]. Therefore, the bubble evolution parameters near the ONB may be good predictors of overall pool boiling performance. The critical heat flux (CHF), an indicator of pool boiling heat transfer capability, is triggered by hydrodynamic instability during pool boiling, scales as:[4]

$$\mathrm{CHF} \sim h_{\mathrm{fg}}\rho_{\mathrm{v}}^{\frac{1}{2}}[\sigma g(\rho_{\mathrm{l}}-\rho_{\mathrm{v}})]^{\frac{1}{4}}, \tag{S5}$$

where h_{fg} denotes the latent heat of evaporation. Comparing with Eqs. (S3) to (S5), one observes that the bubble departure diameter, frequency, and CHF have a relationship with Rayleigh-Taylor instability through the characteristic length $\sqrt{\sigma/[g(\rho_{\mathrm{l}}-\rho_{\mathrm{v}})]}$. The common relationship to the characteristic length indicates that CHF may be correlated with bubble departure diameter and frequency near the ONB.

Furthermore, q'' is equivalent to the heat removal carried off by liquid vaporization, which can be expressed as:

$$q'' = \frac{\pi}{6}h_{\mathrm{fg}}\rho_{\mathrm{v}}fD_{\mathrm{d}}^{3}n, \tag{S6}$$

where n is the active nucleate site density. The nucleation site density is highly depend on surface morphology, liquid properties and wall superheat, and can be described as:[5]

$$n = \varepsilon\left[R_0\frac{\rho_{\mathrm{v}}h_{\mathrm{fg}}}{2\sigma T_{\mathrm{sat}}}\right]^{m}\Delta T_{\mathrm{sat}}^{\mathrm{m}}, \tag{S7}$$

where ε, m are empirical constants[5], R_0 is the upper threshold radius of the cavities on the surface, T_{sat} and ΔT_{sat} denote the saturation temperature and wall superheat, respectively. During nucleate pool boiling, the increase of heat flux only results in the increase of n due to activation of new nucleation sites at elevated ΔT_{sat}.[5,6] The bubble departure diameter and frequency are independent of heat flux, until the generated vapor bubbles transform to vapor column near CHF.[6] Past studies have observed that the heat flux scales well with $\Delta T_{\mathrm{sat}}^{\mathrm{m}}$.[5,7] The bubble departure diameter and frequency, which are considered to remain constants with respect to hydrodynamic instability, are influenced by surface properties. Based on the findings in past

literature, and Eqs. (S4) and (S5), we suspect that CHF on a specific surface scales with f/D_{d}, which are expressed as

$$q''_{\mathrm{CHF}} \sim h_{\mathrm{fg}}(\rho_{\mathrm{v}}\sigma)^{\frac{1}{2}}\left[\frac{\sigma}{g(\rho_{\mathrm{l}}-\rho_{\mathrm{v}})}\right]^{\frac{1}{4}}\frac{1}{D_{\mathrm{d}}} \tag{S8}$$

$$q''_{\mathrm{CHF}} \sim h_{\mathrm{fg}}\left[\frac{\rho_{\mathrm{l}}\rho_{\mathrm{v}}\sigma}{g(\rho_{\mathrm{l}}-\rho_{\mathrm{v}})}\right]^{\frac{1}{2}} f \tag{S9}$$

S8. Durability of the Hierarchical Structured Surfaces

The durability of structured surfaces has always been a key bottleneck to industrial implementation. To increase particle-substrate adhesion, the electrodes were first reversed prior to surface modification by connecting the working sample to the positive potential, and the counter electrode to the negative potential. Then, a very low current (0.1 A/dm^2) was applied for 5 seconds to ensure that the copper sample was activated and the adhesion between the deposited structures and surface is enhanced. To rapidly characterize the durability of our samples, top-view SEM images of the structure after undergoing steady pool boiling for 2 hours revealed negligible difference when compared with the original surfaces (Fig. S7). Longer timescale tests on samples having loner deposition thicknesses would sometimes result in flaking and removal of the structures. To enhance long-term durability, sintering was considered (see Section S9).

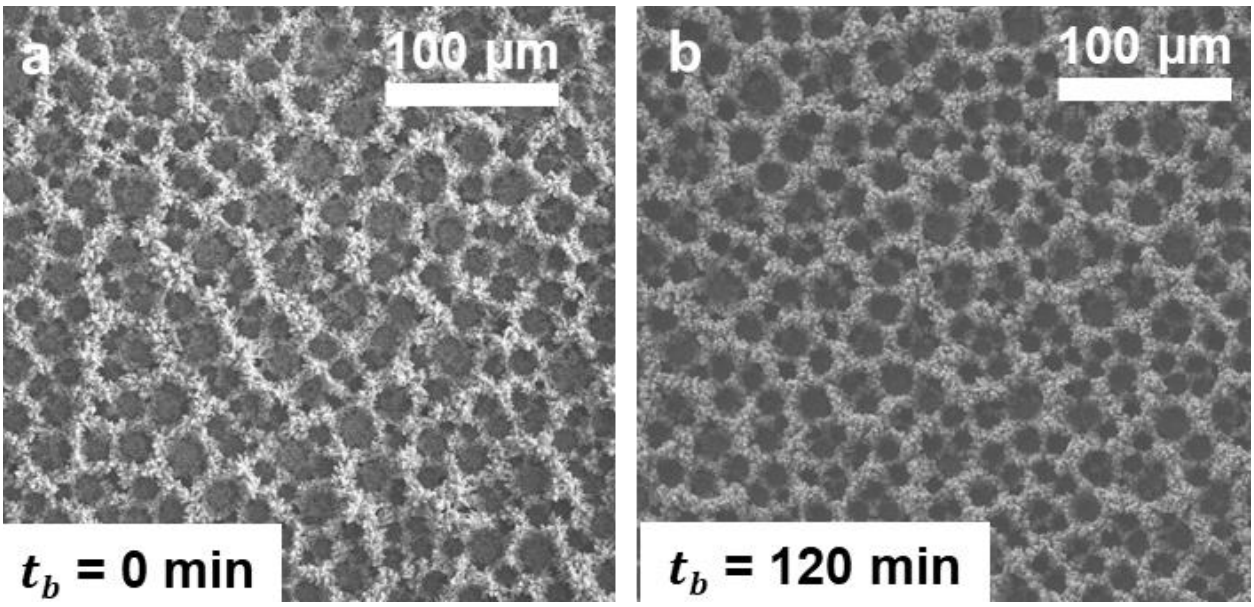

Figure S7. Top-view SEM images of the fabricated hierarchical structured surfaces (a) before and (b) after undergoing pool boiling in water for 2 hours. The hierarchical structures were obtained using a deposition time of 5 s.

S9. Sintering Experiments

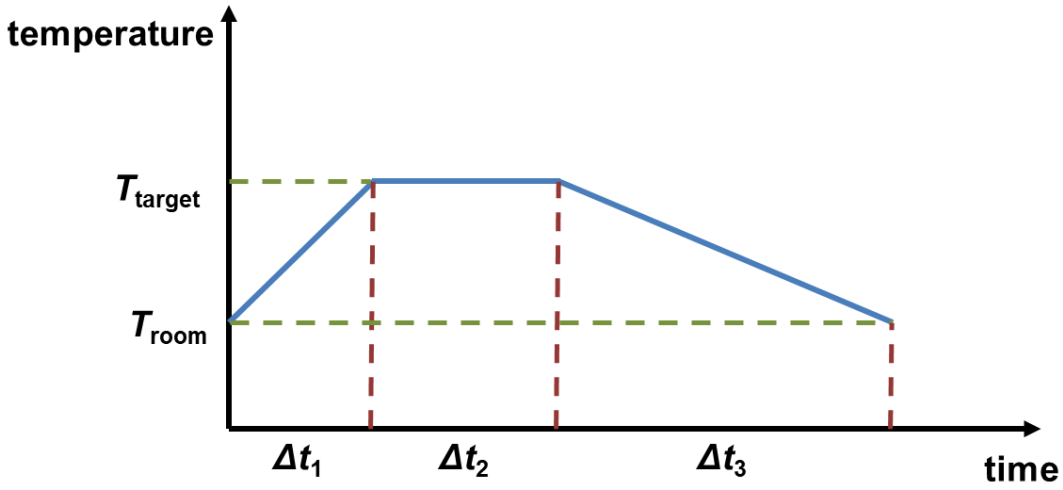

Figure S8. Schematic process diagram of the sintering process.

Table S2. The specific parameter values during sintering

Parameter	T_{room}	T_{target}	Δt_1	Δt_2	Δt_3
Value	25°C	720°C	14 min	20 min (or 120 min)	120 min

S10. Performance of Sintered Surfaces

After sintering, nanoparticles begin to fuse with each other and the number of nanoscale channels decreases, leading to the shrinkage of dendritic structures. The dendritic structures decrease in height while increasing in average pore size, as the sintering time increases. As shown in Fig. R9(a, b), the average pore size on the sintered surfaces ($t_s = 120$ min) increases to 26 μm, 32% higher when compared to the un-sintered surfaces (19.5 μm). Simultaneously, the average height of dendrites decreases from 23 μm to 18.5 μm after sintering.

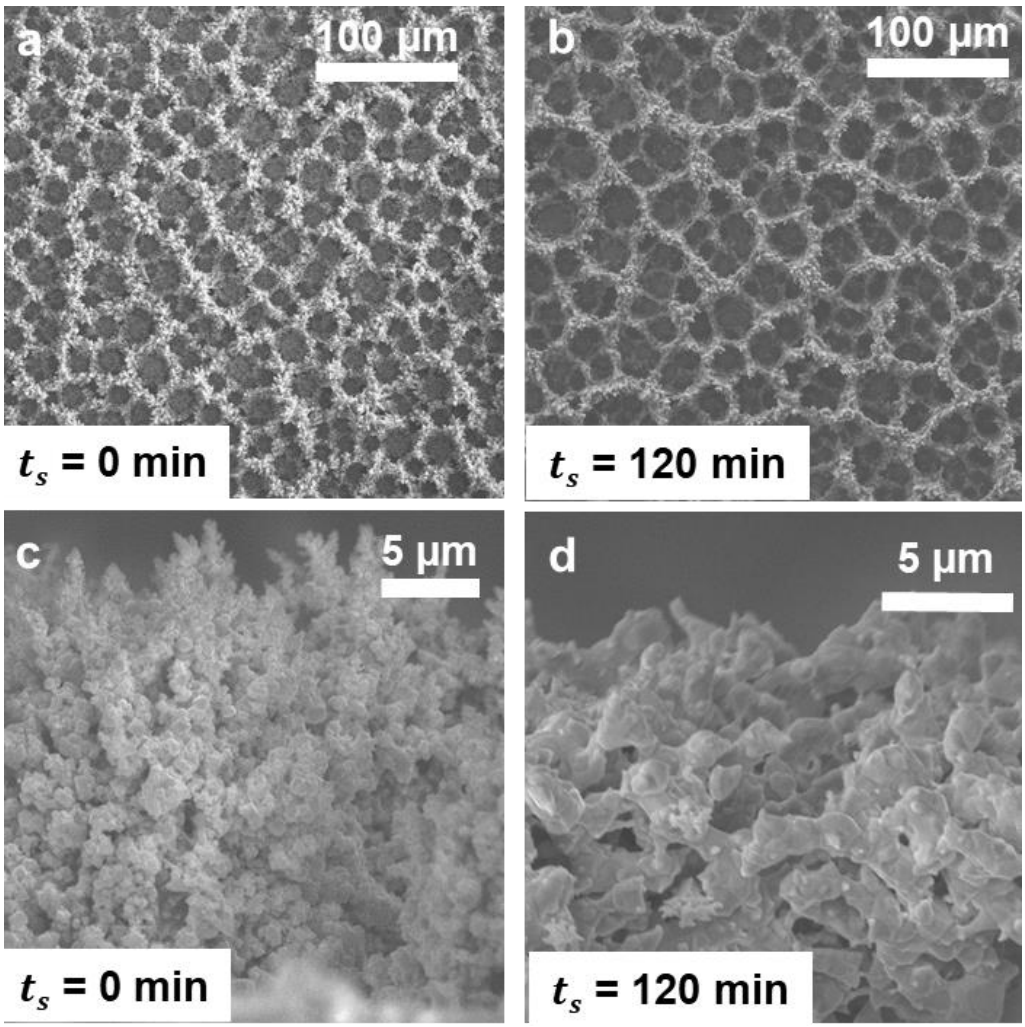

Figure S9. SEM images of the fabricated hierarchical structured surfaces showing the top-view of samples fabricated with sintering times (t_s) of (a) $t_s = 0$ min, and (b) $t_s = 120$ min. Cross-sectional views of samples made with (c) $t_s = 0$ min, and (d) $t_s = 120$ min. All structures were obtained with a deposition time of 5 s.

We also measured the surface wickability of the sintered structures and compared the relationship of Wi number with the CHF enhancement (as observed in Figure 5(a) of the manuscript). The results are shown in Fig. S10. As illustrated in the manuscript, with the increasing sintering time, the nanoparticles fuse with each other and the number of nanoscale channels decreases, leading to a lower ability to absorb water. A comparison of the CHF-Wi results (Fig. S10(b)) among the sintered surfaces (the black and pink data points) and un-sintered surfaces shows that the hierarchical surfaces, after being sintered, fall in line with the obtained CHF-Wi trend.

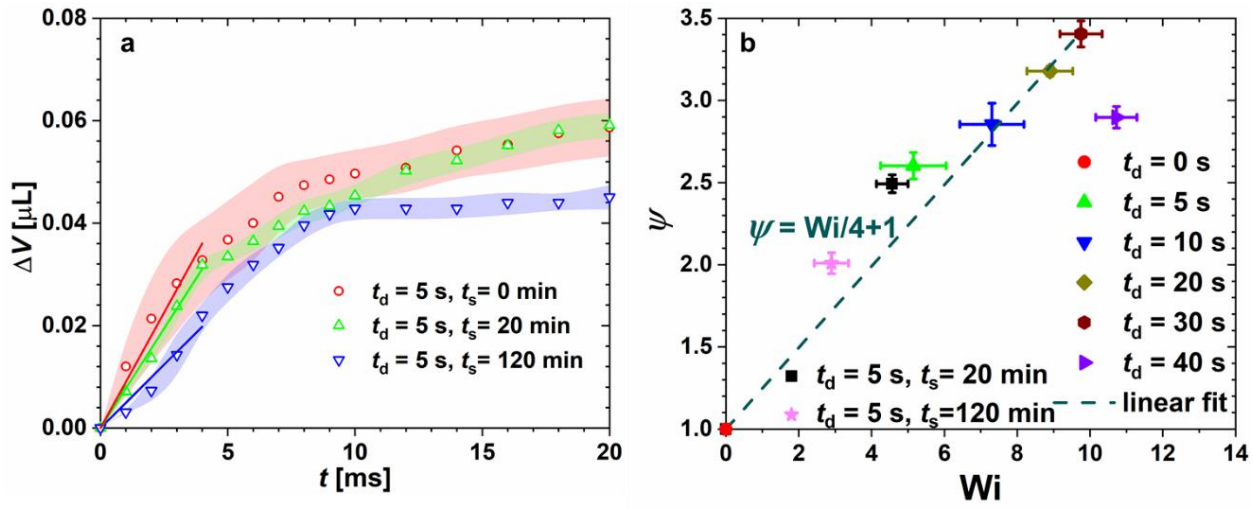

Figure S10. (a) Transient liquid volume absorbed (ΔV) by the hierarchical structured surfaces for a variety of samples made with different sintering times (t_s), and a deposition time t_d of 5 s. (b) CHF enhancement ratio as a function of the dimensionless wicking number.

References

1. Ahn, H. S.; Kim M. H. The Boiling Phenomenon of Alumina Nanofluid near Critical Heat Flux. *Int. J. Heat Mass Transfer* **2013**, *62*, 718-728.
2. Cole, R. Bubble Frequencies and Departure Volumes at Subatmospheric Pressures. *AIChE J.* **1967**, *13*, 779-783.
3. Carey, V. P. *Liquid-Vapor Phase-Change Phenomena: An Introduction to the Thermophysics of Vaporization and Condensation Processes in Heat Transfer Equipment*. 2nd ed.; Taylor and Francis: New York, **2008**; pp 242-267.
4. Kutateladze, S. S. On the Transition to Film Boiling under Natural Convection. *Kotloturbostroenie* **1948**, *3*, 10-12.
5. Mike, B. B.; Rohsenow, W. M.; A New Correlation of Pool-Boiling Data Including the Effect of Heating Surface Characteristics. *J. Heat Transfer* **1969**, *91*, 245.
6. Zuber, N. *Hydrodynamic Aspects of Boiling Heat Transfer*, University of California: Los *Angeles, California,* **1959**
7. Wen, R.; Li, Q.; Wang, W.; Latour, B.; Li, C. H.; Li, C.; Lee, Y.; Yang, R. Enhanced Bubble Nucleation and Liquid Rewetting for Highly Efficient Boiling Heat Transfer on Two-Level Hierarchical Surfaces with Patterned Copper Nanowire Arrays. *Nano Energy* **2017**, *38*, 59-65.